Nanoscale

PAPER

View Article Online
View Journal | View Issue

Cite this: *Nanoscale*, 2025, **17**, 12786

Bi_2Se_3–$PtSe_2$ heterostructure ultrabroadband UV-to-THz negative photoconductive photodetectors with wide-temperature-range operation†

Tianyu Shu,[a] Chao Tan,[a] Guohua Hu,[b] Siyuan Luo[c] and Zegao Wang *[a]

Ultra-broadband photodetectors have important applications in biomedical imaging, environmental monitoring, optical communication, space exploration, and other fields. Therefore, the need for their wide-temperature-range adaptation in extreme environments (*e.g.*, infrared guidance and space exploration) is particularly urgent. However, existing technologies face a number of bottlenecks. First, traditional semiconductor detectors are limited to a single spectral response, meaning ultra-wideband detection requires multi-device integration, while in the terahertz band, there is a physical limitation of the mismatch between the photon energy and the material bandgap. Second, carrier scattering at high temperatures leads to a sudden drop in mobility and degradation of the optical response. Finally, the development of devices based on the negative photoconductivity effect is still in the exploratory stage, which limits their engineering applications. In this study, we innovatively integrated the photothermoelectric effect (PTE), Joule thermal effect (JHE) and photoinduced bolometric effect (PBE) multi-physics mechanisms by constructing a Bi_2Se_3–$PtSe_2$ heterojunction, which realizes broad-spectrum UV–terahertz (405 nm–0.1 THz) detection and stable operation in a wide temperature range of 183–501 K. Under zero bias, the device exhibits a self-powered positive optical response in the 405–1550 nm band based on the photothermoelectric effect. When bias voltage is applied, a negative photoconductive response is triggered by a synergistic Joule heating and optical radiothermal effect, with a peak responsivity (R) of 44.45–83.6 A W^{-1}, specific detection rate (D^*) of up to 4.63×10^7 Jones, and noise-equivalent power (NEP) as low as 1.37×10^{-13} W $Hz^{-1/2}$. Temperature characterization tests show that the R/D^*/NEP was optimized to 78.19 A W^{-1}/5.75×10^7 Jones/1.09×10^{-13} W $Hz^{-1/2}$ under 1550 nm illumination and at 183 K. Even at 501 K, the device maintains 11.24 A W^{-1} responsivity and 7.9×10^6 Jones detection sensitivity. The present work breaks through the limitations of the traditional negative photoconductivity effect in terms of the detection bandwidth and temperature stability through a multi-mechanism synergistic strategy, providing a theoretical basis and technical path for the design of a new generation of broad-spectrum photodetectors.

Received 24th February 2025,
Accepted 23rd April 2025

DOI: 10.1039/d5nr00822k

rsc.li/nanoscale

Introduction

Photodetectors, as the core components of optoelectronic integrated circuits, have important applications in biomedical imaging, environmental monitoring, space remote sensing and high-speed optical communication.[1–5] However, with the growing demand for multi-band spectral analysis, the narrow-band response characteristics of traditional single-band detectors make it difficult to meet the demands of complex scenarios.[6,7] The current mainstream semiconductor material systems face significant technical bottlenecks. For instance, Si[8] and PbS[9] as representative narrow bandgap semiconductors mainly cover visible–near-infrared wavelengths, while they face physical limitations in far-infrared–terahertz wavelengths owing to the mismatch between the photon energy and the bandgap of the materials.[10–14] Although HgCdTe and other materials possess a broad-spectrum response, their liquid-nitrogen-temperature (77 K) operating requirements seriously limit the device miniaturization process.[15] In high-temperature-operating environments (>450 K), traditional germanium-based and InGaAs-based detectors face even more serious challenges: the exponential increase

[a]*College of Materials Science and Engineering, Sichuan University, Chengdu 610065, China. E-mail: zegao@scu.edu.cn*
[b]*Department of Electronic Engineering, The Chinese University of Hong Kong, Shatin, Hong Kong SAR, 999077, China*
[c]*Microsystem and Terahertz Research Center, China Academy of Engineering Physics, Chengdu 610200, China*
† Electronic supplementary information (ESI) available. See DOI: https://doi.org/10.1039/d5nr00822k

in the concentration of thermally excited carriers leads to a significant reduction in carrier mobility and rapid degradation of responsivity and other performance degradation phenomena, and this thermal stability defect has a direct impact on the positioning accuracy of infrared guidance systems and the long-time reliability of deep-space exploration equipment.[16–18] In addition, the current photoelectric detection technology generally adopts the positive photoconductivity (PPC) effect, while the development of devices based on the negative photoconductivity (NPC) effect is still in the exploration stage. Existing NPC studies have tended to focus on three-dimensional (3D) bulk materials, thin-film structures, and nanowire systems, but the low photoelectric conversion efficiency of NPC devices compared to PPC devices has severely limited their practical engineering applications.[19] Therefore, there is an urgent need to develop novel wide-spectrum detectors with superior thermal stability that can effectively suppress thermal carrier scattering, enabling enhanced operating temperature thresholds above 450 K while eliminating the requirement for complex cooling systems. In addition, in-depth study of the mechanism of the negative photoconductivity effect in materials and optimization of the carrier-transport properties are needed and could significantly help to promote the performance breakthrough of NPC optoelectronic devices. This research direction not only fits the priority development areas of the International Roadmap for Semiconductor Technologies (IRDS),[20] but could also provide a new material basis for the design of next-generation high-performance photodetectors.

Two-dimensional (2D) materials and their van der Waals heterostructures provide a promising research platform for developing miniaturized and integrated broadband optoelectronic detection systems. Characterized by atomic-scale thickness, 2D materials exhibit unique mechanical strength, optical response, and electron-transport properties, especially their layer-dependent bandgap tunability, broad spectral absorption capability, and high carrier mobility, which have become cutting-edge hotspots in the research into novel optoelectronic devices.[1,13,18] However, single 2D materials are limited by the constraints of the intrinsic bandgap on the light-absorption efficiency and the fast complex dynamics of the photogenerated carriers, leading to difficulties in improving the photovoltaic conversion efficiency (PCE) and integrating the multidimensional advantages of the broad spectral response, high mobility, and strong exciton effect desired for applications.[21–23] To address this scientific challenge, van der Waals heterointegration technology provides an innovative solution for the construction of multifunctional heterojunctions due to the unique material compatibility advantage demonstrated by its interface without dangling-bond properties.[24] At the heterojunction interface, the spatial separation efficiency of photogenerated carriers can be significantly promoted by regulating the built-in electric field formed by the Fermi energy level difference between the two materials, and this physical mechanism can not only effectively improve the response speed of the device, but also enable realizing a highly efficient operation mode under zero-bias conditions.[25,26] Two-dimensional heterostructures (*e.g.*, $TaSe_2$–graphene,[27] ZrGeSe–graphene,[26] $PtTe_2$–graphene,[28] $SnSe_2$–Bi_2Se_3,[25] BP–MoS_2,[29] $PdSe_2$–$NbSe_2$,[24] Ta_2NiSe_5–graphene,[22] *etc.*) have shown breakthrough potential in the field of UV to terahertz photodetection. Among these, Bi_2Se_3, as a topological insulator, has a certain energy gap in its bulk state itself (the theoretically calculated bulk energy gap is 0.3 eV), and it has been reported that the size of the surface-state energy gap changes with the thickness of the Bi_2Se_3 film. Specifically, as the thickness increases from 2 quintuple layer (QL) to 6 QL, the energy gap gradually decreases, and finally disappears at 6 QL, forming a Dirac cone. This change is correlated with the topological property transition of the film, which is tame for thicknesses less than 6 QL and nontrivial for thicknesses greater than 6 QL, and offers significant advantages in broadband optical detection by virtue of its Dirac surface-state-induced special energy band structure, excellent carrier mobility, and environmental stability.[30–32] Also, the energy band structure of $PtSe_2$ shows significant changes with changes of its thickness. Specifically, for thinner layers, such as 1–2 monolayers (MLs), it has obvious semiconductor properties; then, as the number of layers increases, the energy band structure gradually evolves. When the number of layers is increased to *e.g.*, 5–6 MLs, the energy band structure undergoes an important transformation, and the material gradually transitions from semiconductor to semimetal, with a negative indirect band gap, showing semi-metallic properties with both broad-spectrum absorption and high mobility, suggesting it is a new choice of material for the development of high-performance nanophotovoltaic devices.[18,33–35]Current research has successfully constructed a variety of van der Waals heterojunction photodetectors based on Bi_2Se_3 and $PtSe_2$ (*e.g.*, Bi_2O_2Se–Bi_2Se_3,[30] Bi_2Se_3–Te,[31] $PtSe_2$–BP,[18] $PtSe_2$–$MoSe_2$,[33] $PtSe_2$–Ge[34]), which exhibit excellent performance in the visible to terahertz bands. However, it should be pointed out that the existing Bi_2Se_3-based and $PtSe_2$-based detectors are mainly based on the positive photoconductive (PPC) effect, and their operating temperatures are mostly confined to the room temperature range; while the study of devices with the negative photoconductive (NPC) effect that can work stably at extreme temperatures is still relatively limited; in particular, a means of expanding the negative-responsive waveband to the terahertz frequency domain has not yet been reported in systematic studies.

In this study, we prepared a negative photoconductivity (NPC) effect detector based on a Bi_2Se_3–$PtSe_2$ heterojunction, which could realize an ultra-broad-spectrum photoresponse in the ultraviolet (405 nm) to terahertz (0.1 THz) bands and groundbreakingly extend the operating temperature window to the extreme interval of 183–501 K. Through the synergy of multiple physical mechanisms, the device exhibited excellent performance, including a self-driving capability and high responsivity. At 0 bias voltage, the device exhibited excellent self-driving capability in the 405–1550 nm band. At applied bias, the device demonstrated an enhanced response dominated by the NPC effect in the full UV–terahertz spectral band, with a peak responsivity of 83.6 A W^{-1} in the 0.1 THz band and a noise-equivalent power (NEP) generally lower than 2.61×10^{-13}

W $Hz^{-1/2}$. In the 1550 nm band, when the temperature dropped to 183 K, the responsivity improved to 78.19 A W^{-1}, while the NEP was optimized to 1.09×10^{-13} W $Hz^{-1/2}$, and even at a high temperature of 501 K, a responsivity of 11.25 A W^{-1} could be maintained with a NEP of 8.04×10^{-13} W $Hz^{-1/2}$ and a consistently high signal-to-noise ratio (SNR).

Results and discussion

In this study, Bi_2Se_3–$PtSe_2$ heterojunction photodetectors were successfully prepared. Fig. 1a shows a schematic of the 3D structure of the device and a model illustration of the interface atomic arrangement. The macroscopic morphology of the device was characterized by optical microscopy (Fig. 1b), and its specific preparation process is detailed in the flow schematic of S1.† The heterostructures were morphologically analyzed by atomic force microscopy (AFM) (Fig. 1c), and the thicknesses of the Bi_2Se_3 and $PtSe_2$ nanosheets were measured to be 108 and 213 nm, respectively, which exhibited good laminar structural characteristics. To systematically evaluate the heterojunction interface quality, Raman spectroscopy analysis was further carried out. The characteristic vibrational modes of the Bi_2Se_3, $PtSe_2$ single-component films and their heterostructures are demonstrated comparatively in Fig. 1d. In this figure, it can be seen that the $PtSe_2$ film exhibited typical vibrational peaks at 177.7 cm^{-1} (E_g mode) and 209.7 cm^{-1} (A_{1g} mode); whereas the characteristic peaks of the Bi_2Se_3 film were located at 132.3 cm^{-1} (E_g^2 mode) and 175.5 cm^{-1} (A_{1g}^2 mode), which was consistent with prior literature reports.[25,36] It is noteworthy that in the overlap region of the heterojunction samples, the characteristic peaks of both materials were retained intact and no significant peak shifts were observed, which strongly confirmed the stable binding of Bi_2Se_3 and $PtSe_2$ at the heterojunction interface. The above analytical results indicate that the Bi_2Se_3–$PtSe_2$ heterojunction with good interfacial quality had been successfully constructed in this work, which lays a structural foundation for devices to realize efficient carrier transport and excellent photoresponse performances.

We further investigated the optoelectronic properties of the Bi_2Se_3–$PtSe_2$ heterojunction. Fig. 2a illustrates the current–voltage (I–V) characteristic curves of the heterojunction under 405, 520, 808 and 1550 nm wavelengths under light and dark conditions. The linearly increasing current–voltage relationship confirmed the formation of an ideal Ohmic contact between the device and the metal electrode. In addition, unlike conventional photodetectors, the device exhibited current decay after illumination, suggesting a unique light-response mechanism. Fig. 2b shows that at 1 V bias, the time-resolved photocurrent (I–T) curve of the device exhibited a significant negative photoconductivity (NPC) effect; whereby light illumination at all wavelengths caused the current to drop sharply, which then slowly recovered to the initial state after the light illumination stopped. Under zero-bias conditions (Fig. 2c), on the other hand, the device exhibited a typical posi-

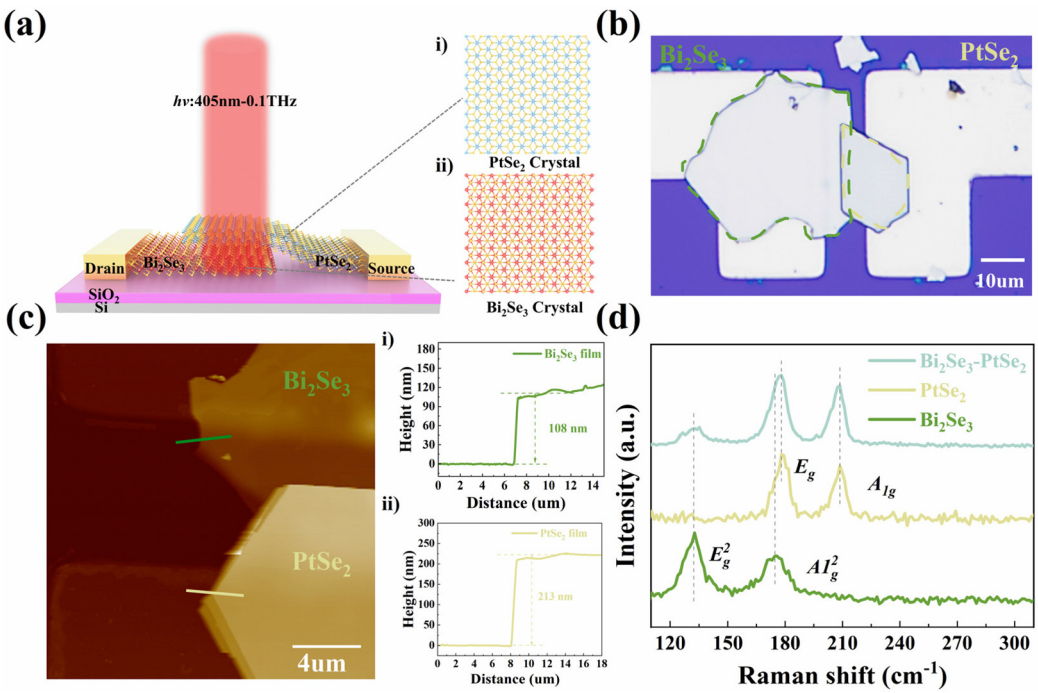

Fig. 1 Schematic structure and material properties of the Bi_2Se_3–$PtSe_2$ heterojunction. (a) Device schematic, (i) schematic of the atomic structure of $PtSe_2$ crystals, (ii) schematic of the atomic structure of Bi_2Se_3 crystals. (b) Optical microscopy image of the Bi_2Se_3–$PtSe_2$ photodetector. (c) AFM image of the Bi_2Se_3–$PtSe_2$ device, (i) indicates that the thickness of Bi_2Se_3 was about 108 nm, and (ii) indicates that the thickness of $PtSe_2$ was about 213 nm. (d) Raman spectra of Bi_2Se_3, $PtSe_2$ and Bi_2Se_3–$PtSe_2$ heterojunctions.

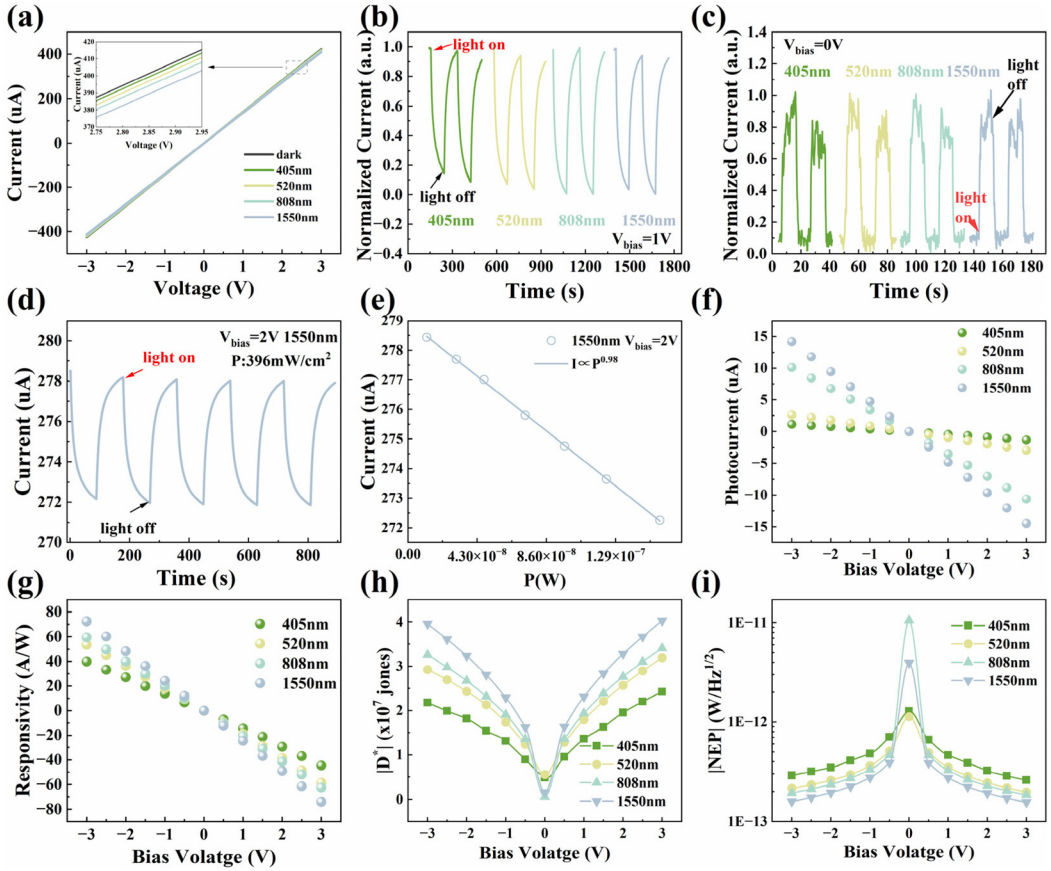

Fig. 2 Photoelectric properties of Bi_2Se_3–$PtSe_2$ heterojunction photodetectors at UV to IR wavelengths. (a) *I*–*V* characteristic curves of the device under different-wavelength irradiation and in the dark state. Optical response of the device under 405–1550 nm wavelength irradiation at (b) V_{bias} = 1 V and (c) V_{bias} = 0 V. Stability curves of the photocurrent of the device under 1550 nm illumination (d) and the fitted curves of the current *versus* the power intensity (e), V_{bias} = 2 V. Photocurrent (f), responsivity (g), specific detectivity (h), and noise-equivalent power (i) *versus* bias voltage for devices irradiated at 405–1550 nm.

tive photoconductance (PPC) effect, whereby the current increased significantly with light and gradually recovered after the light illumination stopped. This phenomenon of the coexistence of positive and negative photoresponse stemmed from the synergistic effect of different mechanisms within the heterojunction. The large dark current, among others, may have been caused by the coupling effect between the metallic properties of the surface states of the Bi_2Se_3 topological insulator and the semi-metallic nature of $PtSe_2$.[33,37] The time-resolved photocurrent response tests (Fig. S2†) revealed that the photocurrent at 1 V bias showed systematic attenuation when the optical power density was increased, and this negative photoresponse feature was consistent with the NPC effect mechanism. Fig. 2d demonstrates the *I*–*T* curves for 2 V bias under 1550 nm laser irradiation, confirming the excellent stability and cycling reliability of the device. The linear dynamic range analysis (Fig. 2e and S3†) showed that the photocurrent exhibited a good linear relationship with the incident optical power ($I \propto P^{\theta}$, $\theta \approx 1$), displaying excellent linear response characteristics. In addition, under the zero-bias condition (Fig. S4†), the heterojunction exhibited a high signal-to-noise ratio and fast response characteristics in the full wavelength range of 405–1550 nm, with the corresponding rise/decay times at each wavelength as follows: 405 nm (0.95/0.83 ms), 520 nm (0.98/0.88 ms), 808 nm (0.93/0.82 ms), 1550 nm (0.96/0.85 ms). Fig. 2f reveals the linear modulation property of the photocurrent with the bias voltage, which provides an important basis for device performance optimization. By systematically characterizing the optoelectronic parameters (Fig. 2g–i), the key performance indexes of the devices were quantified; namely responsivity (R) peaks up to 44.45, 58.51, 62.43, and 73.77 A W^{-1}, respectively, in the 405–1550 nm band; a specific detection rate (D^*) up to 4.03×10^7 Jones; and noise-equivalent power (NEP) as low as 1.57×10^{-13} W $Hz^{--1/2}$. The formulas for determining these parameters are given below:[13]

$$R = \frac{I_{ph}}{P_{in}} = \frac{I_{light} - I_{dark}}{P_{in}}$$

$$D^* = \frac{R\sqrt{A}}{\sqrt{2eI_{dark}}}$$

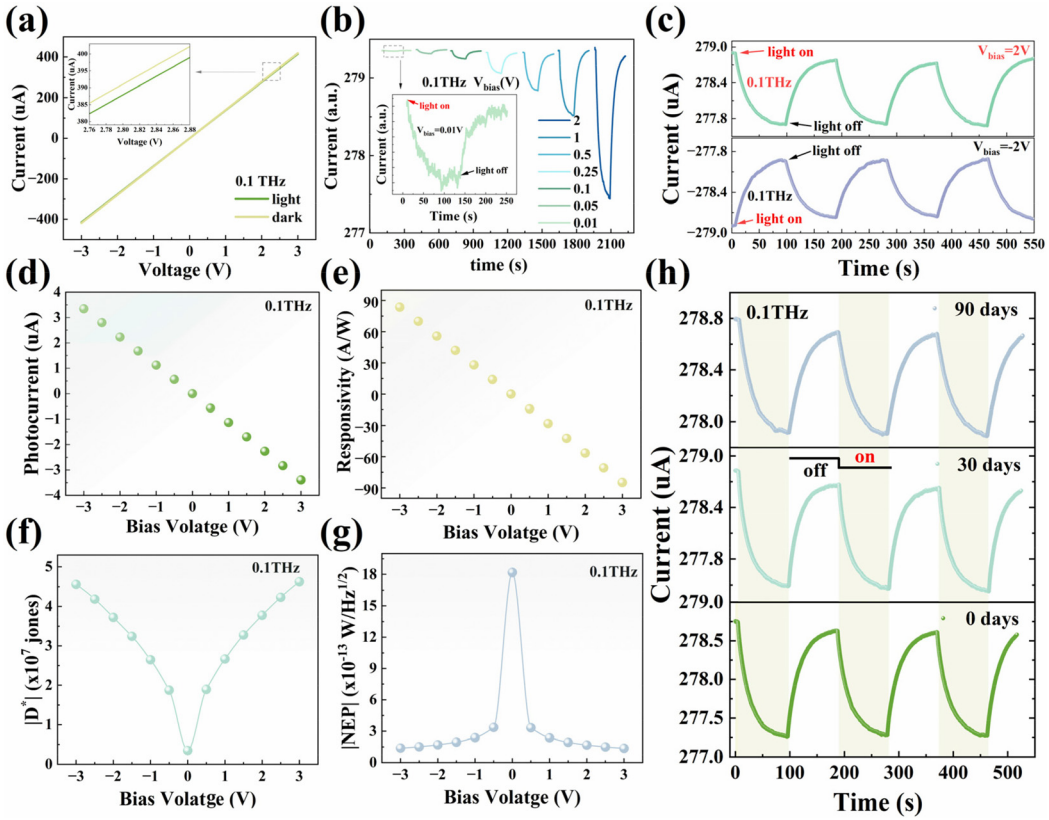

Fig. 3 Photoelectric characterization of Bi_2Se_3–$PtSe_2$ heterojunction photodetectors at 0.1 THz wavelength. (a) Current–voltage (*I*–*V*) characteristic curves of the device under 0.1 THz light and dark conditions. Response curves of the device to the photocurrent at different bias voltages (b) and symmetric response characteristic curves at V_{bias} = ±2 V bias (c). Photocurrent (d), responsivity (e), specific detectivity (f), and noise-equivalent power (g) of the device as a function of bias voltage under 0.1 THz illumination. (h) Long-term stability test curve of the device under 0.1 THz light, V_{bias} = 2 V.

$$\mathrm{NEP} = \frac{\sqrt{AB}}{D^*}$$

where P_{in} is the incident optical power, A (~40 μm^2) is the effective area, e is the *meta*-charge, and B (1 Hz) is the bandwidth. The above results show that the Bi_2Se_3–$PtSe_2$ heterojunction photodetector exhibited excellent comprehensive performance in the UV–infrared broad-spectrum range, while its fast response, high sensitivity, and wide dynamic range characteristics provide an important reference for the development of a new generation of broad-spectrum photodetectors.

In order to further explore the photoresponsivity of the Bi_2Se_3–$PtSe_2$ heterojunction photodetectors in a wider range of wavelength bands, the photoelectric characteristics of the Bi_2Se_3–$PtSe_2$ devices were investigated under 0.1 THz illumination. Fig. 3a demonstrates the current–voltage (*I*–*V*) characteristic curves of the devices under 0.1 THz illumination and dark conditions, and the linear Ohmic characteristics were consistent with the results of the previous UV–IR band studies. The unique negative photoresponse characteristics were still maintained under 0.1 THz illumination, which further validates the universality of the unconventional photoresponse mechanism of this heterojunction. By applying a small bias voltage test (Fig. 3b), it was found that the device exhibited a stable negative photoconductive response (NPC) and high signal-to-noise ratio even at an ultra-low bias voltage of 0.01 V. The excellent performance demonstrated by the device can be attributed to multiple key factors. From a structural point of view, the crystal structure of the material and the stable device structure provide a solid foundation; while at the level of charge transport and interaction, the efficient carrier transport at the heterojunction and the enhanced interfacial coupling play a key role in improving the device performance.[25,26] Fig. 3c reveals the symmetric response of the device at ±2 V bias with >95% waveform fidelity for both positive and negative bias, which was attributed to the quasi-metallic contact property of the heterojunction. The photocurrent-bias relationship study (Fig. 3d) showed the excellent linear correlation between the photocurrent and bias voltage in the range of ±3 V, demonstrating the effective regulation of carrier transport by the electric field. Characterization of the key performance parameters (Fig. 3e–g) showed that an ultra-high responsivity of 83.6 A W^{-1} was obtained at −3 V bias, which was 3 orders of magnitude higher than that of similar terahertz detectors;[22] while a specific detectivity of 4.63 × 10^7 Jones and a noise-equivalent power of 1.37 × 10^{-13} W Hz$^{-1/2}$ were also achieved at 3 V

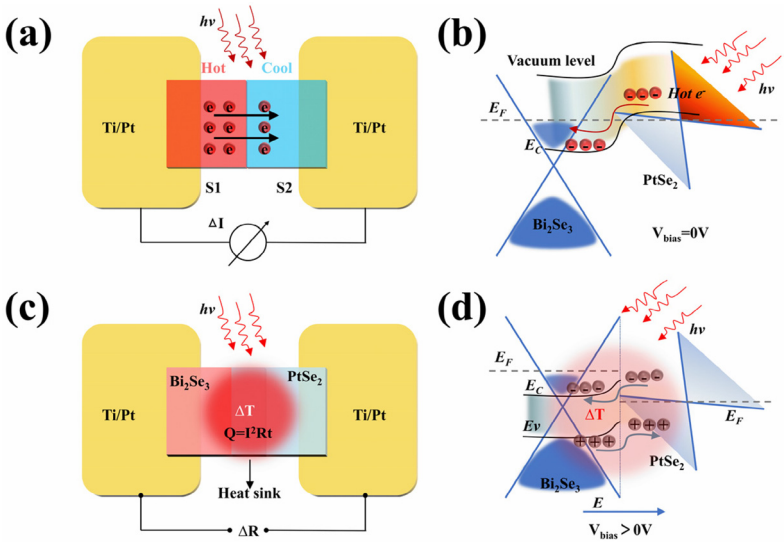

Fig. 4 Photoresponse mechanism of Bi_2Se_3–$PtSe_2$ heterojunction photodetectors. (a) and (b) At V_{bias} = 0 V, the device responds to the mechanism based on the photothermoelectric effect. (c) and (d) At V_{bias} > 0 V, the device responds to the mechanism based on the Joule and photovoltaic thermal effects.

bias. Long-term stability tests (Fig. 3h) showed that the performance of the unpackaged device displayed little degradation after 90 days of exposure to ambient atmospheric conditions, which could be attributed to the intrinsic resistance of the Bi_2Se_3 topological surface state to oxidation, the chemical stability of the $PtSe_2$ layer in air, and the suppression of water molecule penetration by the atomically flat interface. This property is significantly superior to conventional semiconductor material devices. As shown in Fig. S6,† under the same test conditions, devices 2–4 all exhibited consistent negative optical response characteristics with the prototype device (device 1), and the deviations of their R, D^*, and NEP parameters were less than 15%, indicating that the device structure offers good process repeatability. This study demonstrates for the first time the excellent negative photoconductivity performance of the Bi_2Se_3–$PtSe_2$ heterojunction in the terahertz band, and its broad-spectrum response (UV–terahertz), excellent environmental stability, and electrically tuneable properties, which can provide innovative solutions for the development of a new generation of broad-spectrum photodetectors.

In this study, Bi_2Se_3–$PtSe_2$ heterojunction photodetectors were successfully prepared, and the self-driven operation mode of the devices was realized through material energy band engineering. Theoretical analyses and experimental results showed that the photoelectric response of the devices under zero-bias voltage conditions mainly originated from the physical mechanism of the photothermoelectric effect (PTE) (Fig. 4a and b). Specifically, the significant difference in thermal conductivity between Bi_2Se_3 and $PtSe_2$ creates an asymmetric contact structure at the interface of the heterojunction, effectively breaking the mirror-symmetric electric field distribution in conventional devices. When the incident optical radiation is absorbed by the heterojunction, due to the difference in Seebeck coefficients ($\Delta S(E_F)$) between the two materials at the Fermi energy level, the phototropic temperature gradient drives the directional diffusion of carriers from the hot end to the cold end, which generates a thermoelectric potential, $V(x) = -\int \Delta S(E_F)\Delta T(x)\,dx$, which is proportional to the temperature gradient. This self-built electric field drives the directional migration of nonequilibrium carriers, resulting in a self-driven photocurrent $I_{PTE} = \frac{S_1 - S_2}{R}\Delta T(x)$, where R is the total system resistance.[22] The experimental data showed that the heterojunction device exhibited a significant positive photoresponse in a wide spectral range from 405 nm to 1550 nm, which was attributed to the special energy band structure of the $PtSe_2$ semimetal: on the one hand, its work function property effectively improves the interfacial contact between the two-dimensional material and the metal electrodes, which reduces the contact resistance; on the other hand, its narrow bandgap feature significantly enhances the photonic response in the near-infrared band (especially at 1550 nm) and photon-absorption efficiency, which extends the device response spectral range to the communication band. Notably, the high thermal conductivity of Bi_2Se_3 and the moderate thermal conductivity of $PtSe_2$ form an effective thermal resistance difference, which can generate a higher temperature gradient than for the same types of devices at the same optical power density, which is a key factor for realizing an efficient PTE effect. This PTE modulation strategy based on heterojunction interface engineering provides an important theoretical basis for the design of a new generation of self-driven photodetectors.

This study further revealed the photoresponse mechanism of the Bi_2Se_3–$PtSe_2$ heterojunction under bias voltage. It was

shown that the negative photoresponsive behaviour of the device originated from the synergistic effect of the Joule thermal effect (JHE) and photoinduced bolometric effect (PBE) when an external electric field was applied (Fig. 4c and d). The topologically protected metallic state of the Bi_2Se_3 surface and the $PtSe_2$ semi-metallic properties formed a composite channel system with a significant sensitivity of its resistance to temperature variations (Fig. 5a–c). Specifically, the Joule heating effect can be quantitatively described by the equation $Q_{JH} = \left(\frac{V_{bias}{}^2}{R_{eff}}\right)t$, where V_{bias} is the bias voltage, R_{eff} is the effective channel resistance, and t is the duration.[38] This effect resulted in a sustained temperature rise as current passed through the channel under the no-light conditions, and the system entered thermal saturation when the device heat generation rate reached dynamic equilibrium with the ambient heat dissipation rate (~110 s) (Fig. 5d-I). The PBE effect[13] triggered by the absorption of photon energy by the device under the action of optical radiation can be expressed as $R_h = \frac{dT}{dP}$ (where dP is the optical power absorption, and dT is the corresponding temperature rise), which determines the sensitivity of the device, as well as the thermal capacitance, C_h, which determines the response time of the device, as $\tau = R_h C_h$. This temperature-sensitive resistive modulation mechanism allowed the device to exhibit a significant response even in the 0.1 THz band where the photon energy was significantly lower than the material bandgap (Fig. 5d-II). In addition, the photocurrent exhibited a quasi-linear variation property with the bias voltage when the two thermal effects were combined (Fig. 2f and 3d), a phenomenon that stemmed from the quadratic growth of the Joule thermal power due to the increase in the bias voltage and the enhanced electric field, which accelerated the relaxation process of the hot carriers. As shown in Fig. 5-III, the kinetic process for current recovery in the device after light withdrawal (about 100 s) revealed the correlation between the thermal relaxation time constant and parameters such as the material heat capacity and interface thermal resistance.

Photodetectors based on conventional semiconductor materials exhibit significant intrinsic carrier concentration decay in low-temperature environments, which stems from the reduced generation of electron–hole pairs due to the decrease in thermal excitation energy.[18] In contrast, at high temperatures, the photogenerated carrier-transport process is signifi-

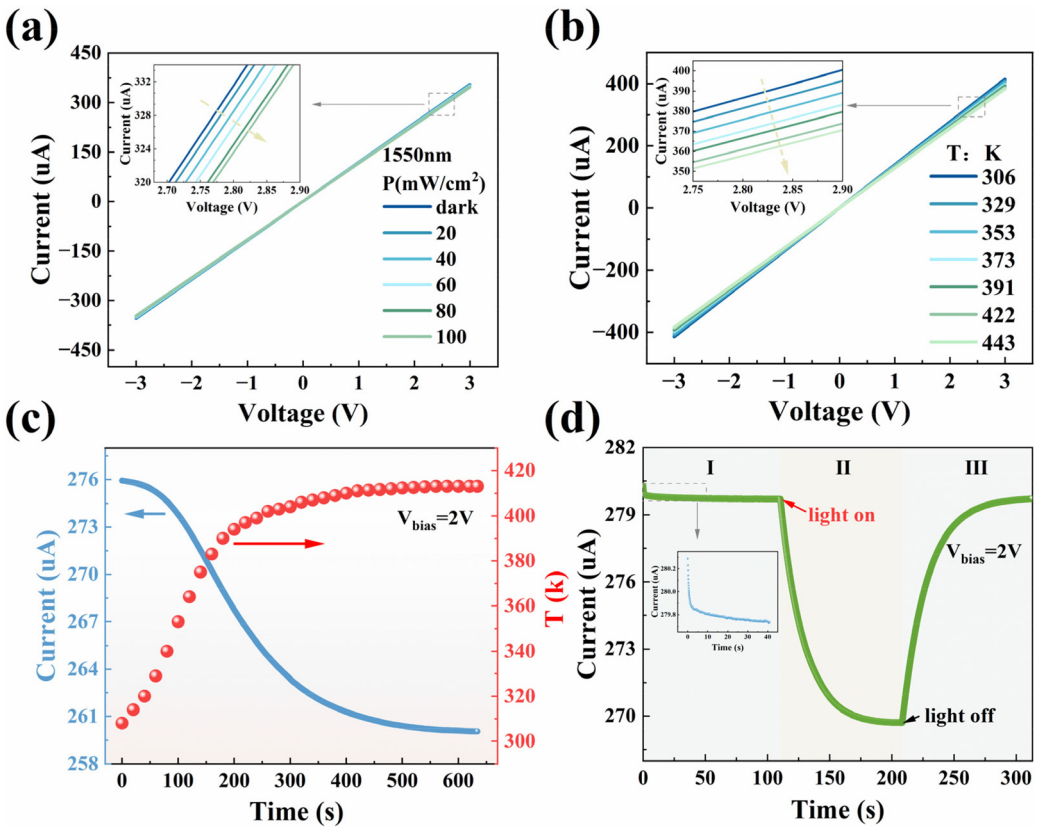

Fig. 5 Negative photoresponse characteristics of Bi_2Se_3–$PtSe_2$ heterojunction photodetectors and the whole process of their photocurrent generation. *I*–*V* characteristic curves for different optical power densities (a) and different temperatures under 1550 nm illumination (b). The current generated by the device gradually decreased when the light intensity increased, and the resistance increased accordingly. At the same time, with the increase in temperature, the trend for the device current was the same as that for the increase in light intensity. (c) Curves of the current of the device as a function of temperature in the absence of light. The curves show that the temperature change caused a change in the current of the device and the current tended to decrease as the temperature increased. (d) The entire process of photocurrent generation, V_{bias} = 2 V.

cantly affected by lattice vibrations (phonon scattering), and the mobility is degraded by an exponential increase in the scattering probability, while the contribution of impurity scattering exhibits a non-monotonic variation with increasing temperature (dominant in the low-temperature region but masked by phonon scattering in the high-temperature region).[39] The above temperature-dependent carrier dynamics leads to photocurrent amplitude attenuation and an elevation of the noise floor at extreme temperatures, ultimately triggering a significant degradation of the signal-to-noise ratio (SNR). In contrast, photodetectors based on 2D layered materials (*e.g.*, transition metal sulfur compounds) exhibit unique temperature adaptability advantages (Fig. 6a). First, the atomic-level thickness of the 2D materials endows them with a high intrinsic mobility and a weak phonon-coupling property, which effectively suppresses the lattice scattering at high temperatures. Second, interfacial engineering of a van der Waals heterojunction can construct a built-in electric field to separate the photogenerated carriers through the space charge region and reduce the non-radiative composite probability. Third, the defect passivation effect at the heterojunction interface reduces the impurity scattering centre density, thus maintaining carrier-transport efficiency over a wide temperature domain.

In order to evaluate the effective operating temperature range, the photoresponse performance of Bi_2Se_3–$PtSe_2$ devices with increasing temperature was investigated. Fig. 6b and c show the current–time (I–T) curves of the Bi_2Se_3–$PtSe_2$ devices under a V_{bias} of 2 V and 1550 nm light irradiation when the operating temperature was increased. An excellent negative photoresponse performance was demonstrated over the wide operating temperature range of 183 K to 501 K, showing a high signal-to-noise ratio in the waveforms with a stable response pulse. Fig. 6d shows the variation of the photocurrent and responsivity of the device with temperature, from which it can be seen that the photocurrent and responsivity decreased as the temperature increased. The photocurrent and responsivity of the device could reach 23.39 μA and 78.19 A W^{-1}, respectively, at an operating temperature of 183 K. Even at an operating temperature of 501 K, the photocurrent and responsivity could still reach 3.37 μA and 11.25 A W^{-1}, respectively. Fig. 6e shows the specific detectivity and noise-equivalent power of the device *versus* temperature, with the specific D^* and NEP reaching 5.75×10^7 Jones and 1.09×10^{-13} W $Hz^{-1/2}$, respectively, at an operating temperature of 183 K. Even when the operating temperature reached 501 K, the specific detectivity and noise-equivalent power still reached 7.9×10^6 Jones and 8.04×10^{-13} W $Hz^{-1/2}$, respectively. To further demonstrate the photodetection performance of our devices at extreme temperatures, we compared the performance of our prepared Bi_2Se_3/$PtSe_2$ photodetectors with previously reported photodetectors. As shown in Table 1, our devices were able to achieve greater responsivity over a wider temperature range, indicating their high signal-to-noise ratios in extreme temperature environments and great potential applications in areas such as infrared imaging.

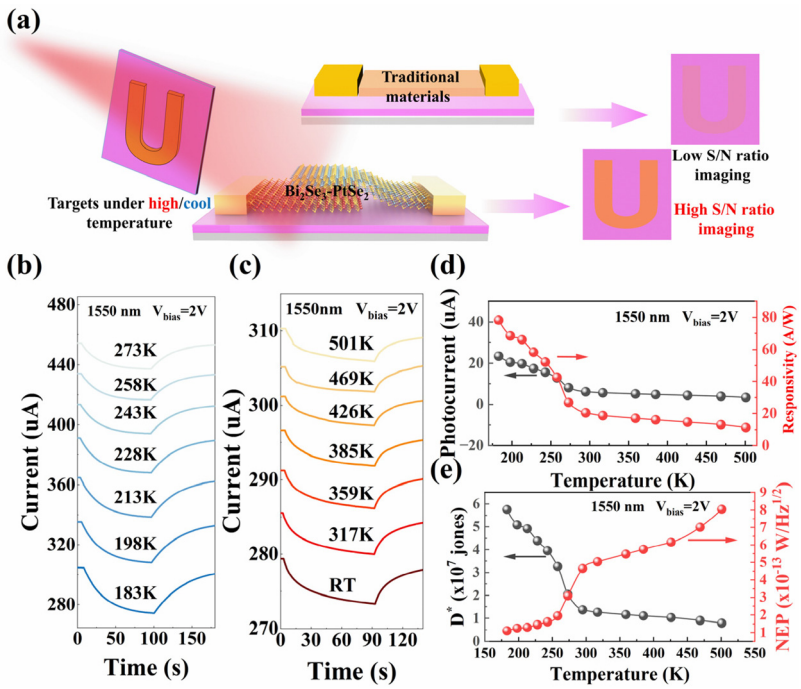

Fig. 6 Photoresponse performance of Bi_2Se_3–$PtSe_2$ heterojunction photodetectors with increasing temperature. (a) Schematic representation of the signal-to-noise ratio (S/N) of Bi_2Se_3–$PtSe_2$ heterojunction devices *versus* conventional devices in high/low-temperature environments. (b) and (c) Photocurrents generated by the device at different operating temperatures, V_{bias} = 2 V, λ = 1550 nm. (d) and (e) Device photocurrent, responsivity, specific detectivity, and noise-equivalent power as a function of temperature.

Table 1 Comparison of the performances of different photodetectors

Material	Response range	Wavelength	Temperature (K)	R (A W^{-1})	D^* (Jones)	NEP (W Hz$^{-1/2}$)	Photoresponse	Ref.
Bi_2Se_3	1456 nm	1456 nm	300	2.74	3.3×10^{10}	—	PPC	37
SnTe–Bi_2Se_3	1550 nm	1550 nm	300	0.15	1.15×10^{10}	—	PPC	40
$PtSe_2$–GaAs	254–1200 nm	808 nm	300	0.26	2.52×10^{12}	—	PPC	23
Graphene/$PtSe_2$/ pyramid Si	980 nm–10.6 μm	10.6 μm	300	0.53	8.4×10^{8}	—	PPC	41
Bi_2Te_3–Si	370 nm–118 μm	635 nm	300	1	—	—	PPC	42
MoS_2	980 nm	980 nm	300	2.3	—	—	NPC	43
Graphene–*p*-Si	1064 nm	1064 nm	300	125	—	—	NPC	44
Bi_2Se_3–Sb_2Se_3	532–1064 nm	1064 nm	300	0.015	2.5×10^{9}	—	NPC	21
$Ir_{1-x}PtxTe_2$–graphene	0.12–0.3 THz	0.12 THz	300	0.52	—	2.40×10^{-11}	PPC	45
$PdSe_2$	405 nm–0.03 THz	0.03 THz	300	0.4	—	5.60×10^{-11}	PPC	46
Ta_2NiSe_5–graphene	638 nm–0.12 THz	0.12 THz	300	0.04	—	2.30×10^{-11}	PPC	22
Bi_2Se_3–$PtSe_2$	405 nm–0.1 THz	1550 nm	501	11.25	7.87×10^{6}	8.04×10^{-13}	NPC	This work
		0.1 THz	300	83.6	4.56×10^{7}	1.37×10^{-13}	NPC	

Conclusions

In conclusion, the Bi_2Se_3–$PtSe_2$ heterojunction photodetector designed in this study based on the synergistic effect of multiple mechanisms exhibited excellent temperature adaptability and an ultra-wideband detection capability. The device could maintain stable operating characteristics over a wide temperature range of 183–501 K and exhibited a unique negative photoresponse behavior in the UV to terahertz band (405 nm to 0.1 THz). Experimental investigations showed that at zero-bias voltage, the photodetection mechanism of the device in the UV to IR range (405–1550 nm) was mainly determined by the photothermoelectric effect (PTE) and it possessed a good self-powered performance. Under applied bias voltage, the photodetection mechanism of the device in the UV to terahertz range (405 nm to 0.1 THz) was mainly determined by the Joule thermal effect and the photothermal effect (PBE), and the device had optimal R, D^* and NEP values of 83.6 A W^{-1}, 4.63×10^7 Jones and 1.37×10^{-13} W Hz$^{-1/2}$, respectively, when exposed to 0.1 THz light. When a bias voltage of 2 V was applied, the R, D^*, and NEP were further optimized to 78.19 A W^{-1}, 5.75×10^7 Jones, and 1.09×10^{-13} W Hz$^{-1/2}$ under 1550 nm illumination and 183 K operating temperature. Even at a high temperature of 501 K, it still maintained a high response of 11.24 A W^{-1}, a detection sensitivity of 7.9×10^6 Jones and a low noise level of 8.04×10^{-13} W Hz$^{-1/2}$, highlighting its extreme-environment adaptability advantages. By systematically analyzing the optical–thermal–electrical coupling mechanism, the central role of the negative photoconductivity (NPC) effect in expanding the detection bandwidth and enhancing the temperature robustness was revealed, and the effect provides a new idea for the dimensional modulation of photodetection systems. This study not only confirms the outstanding potential of the Bi_2Se_3–$PtSe_2$ heterojunction in ultra-wideband detection and wide-temperature applications, but also opens up an innovative path for the development of a new generation of high-performance optoelectronic devices.

Experimental section

Bi_2Se_3–$PtSe_2$ heterojunction photodetectors were prepared as follows (Fig. S1†): n-type doped silicon wafers, for use as the substrate (thickness of the surface thermally oxidized SiO_2 layer of 285 nm), were pretreated by a standard cleaning process, and then placed in anhydrous ethanol, acetone, and isopropanol for ultrasonic cleaning in sequence (15 min each), and the process was repeated twice to thoroughly remove all organic contaminants. The samples were dried under a nitrogen stream and subsequently transferred into a glove box filled with high-purity nitrogen for storage until further use. The metal electrodes were prepared by maskless lithography combined with electron beam evaporation: first, the photoresist was spin-coated on the surface of the silicon wafer, and the electrode pattern was formed after alignment, exposure and development. Subsequently, the substrate was placed in the vacuum chamber of the electron beam evaporation system (background vacuum of 4.5×10^{-4} Pa), and a 10 nm titanium (Ti) adhesion layer and a 20 nm platinum (Pt) conductive layer were deposited sequentially, and the designed electrodes were finally obtained by the lift-off process.

The electrodes with completed metal deposition were then subjected to a lift-off process and impregnated with acetone solution for 10 min to remove the residual photoresist. Two-dimensional Bi_2Se_3 nanosheets were prepared by a mechanical stripping technique, and the selected nanosheets were accurately localized to the electrode functional area by a polycarbonate (PC) film-assisted dry transfer technique, followed by the sequential use of chloroform dissolution to remove the PC carrier film, isopropanol to clean the interfacial contaminants, and nitrogen blow-drying, and then repeating the above process to transfer the $PtSe_2$ nanosheets. In order to optimize the contact characteristics of the heterojunction interface, the devices were annealed in a tube furnace; whereby the devices were annealed in an Ar/H_2 gas mixture (10 : 1 by volume, total flow rate of 220 sccm) at a constant temperature of 250 °C for 1 h. Fig. 1b shows the optical microstructures of the annealed

devices, showing that a clear heterointerface was formed between the Bi_2Se_3 and the $PtSe_2$ nanosheets on the surface of the electrodes. All the tests were conducted in a room temperature environment (~300 K) unless otherwise detailed in the text.

Author contributions

Z. W. conceived, designed and supervised the project. T. Y., C. T., G. H. and S. L. conducted the experimental work and performed the data analysis. T. Y. and Z. W. wrote the manuscript. All the authors contributed to discuss the results and edit the manuscript.

Data availability

The data supporting this article have been included as part of ESI.†

Conflicts of interest

There are no conflicts to declare.

Acknowledgements

This work was financially supported by the National Natural Science Foundation of China (52272160, U2330112), Sichuan Science and Technology Foundation (2025YFHZ0102, 2023YFSY0002, 2024JDRC0021), National Key Research and Development Program of China (2024YFA1209300) and the foundation of Key Laboratory of Lidar and Device, Sichuan Province (Grant No. LLD2023-006).

References

1 J. X. Liu, Z. H. Peng, C. Tan, L. Yang, R. D. Xu and Z. G. Wang, *Front. Phys.*, 2024, **19**, 26.
2 C. Tan, H. J. Wu, Z. C. Lin, L. Yang and Z. G. Wang, *Adv. Funct. Mater.*, 2024, **35**, 2415360.
3 C. Tan, Z. H. Yang, H. J. Wu, Y. Yang, L. Yang and Z. G. Wang, *Nanoscale*, 2024, **16**, 6241–6248.
4 S. Q. Xiao, J. L. Qi, Y. Wang, G. L. Hu, Y. Qin, Z. Z. Cheng, Z. Y. Zhang, Q. Y. He and H. K. Tsang, *Nanoscale*, 2024, **16**, 22423–22429.
5 J. R. Zheng, E. M. You, Y. F. Hu, J. Yi and Z. Q. Tian, *Nanoscale*, 2023, **15**, 8863–8869.
6 D. Wang, C. Tan, H. J. Wu, L. Yang and Z. G. Wang, *Appl. Phys. Lett.*, 2024, **124**, 5.
7 Y. Zhang, J. Wu, L. Jia, D. Jin, B. Jia, X. Hu, D. Moss and Q. Gong, *npj Nanophoton.*, 2024, **1**, 28.
8 J. T. Lu, L. J. Zhang, C. R. Ma, W. J. Huang, Q. J. Ye, H. X. Yi, Z. Q. Zheng, G. W. Yang, C. A. Liu and J. D. Yao, *Nanoscale*, 2022, **14**, 6228–6238.
9 Z. W. Ren, J. K. Sun, H. Li, P. Mao, Y. Z. Wei, X. H. Zhong, J. S. Hu, S. Y. Yang and J. Z. Wang, *Adv. Mater.*, 2017, **29**, 7.
10 Z. Dong, W. L. Guo, L. B. Zhang, Y. Zhang, J. Chen, L. Y. Huang, C. Chen, L. Yang, Z. Q. Ren, J. R. Zhang, W. Z. Yu, J. Li, L. Wang and K. Zhang, *Adv. Sci.*, 2022, **9**, 9.
11 Z. Dong, W. Z. Yu, L. B. Zhang, L. Yang, L. Y. Huang, Y. Zhang, Z. Q. Ren, H. R. Mu, C. Chen, J. R. Zhang, J. Li, L. Wang and K. Zhang, *InfoMat*, 2023, **5**, 11.
12 Y. He, L. Yang, Z. Hu, L. B. Zhang, X. K. Pan, Y. D. Wei, S. G. Guo, X. Y. Lv, M. J. Jiang, L. Han, D. Wang, S. Q. Lan, X. Sun, X. S. Chen, K. Zhang and L. Wang, *Adv. Funct. Mater.*, 2024, **34**, 10.
13 Q. X. Qiu and Z. M. Huang, *Adv. Mater.*, 2021, **33**, 19.
14 D. Wang, L. Yang, Z. Hu, F. Wang, Y. G. Yang, X. K. Pan, Z. Dong, S. J. Tian, L. B. Zhang, L. Han, M. J. Jiang, K. Q. Tang, F. X. Dai, K. Zhang, W. Lu, X. S. Chen, L. Wang and W. D. Hu, *Nat. Commun.*, 2025, **16**, 10.
15 W. J. Liu, Y. Y. Yu, M. Peng, Z. H. Zheng, P. C. Jian, Y. Wang, Y. C. Zou, Y. M. Zhao, F. Wang, F. Wu, C. Q. Chen, J. N. Dai, P. Wang and W. D. Hu, *InfoMat*, 2023, **5**, 31.
16 D. Akinwande, C. Huyghebaert, C. H. Wang, M. I. Serna, S. Goossens, L. J. Li, H. S. P. Wong and F. H. L. Koppens, *Nature*, 2019, **573**, 507–518.
17 C. H. Liu, Y. C. Chang, T. B. Norris and Z. H. Zhong, *Nat. Nanotechnol.*, 2014, **9**, 273–278.
18 X. Yang, X. Zhou, L. Li, N. Wang, R. Hao, Y. A. Zhou, H. Xu, Y. T. Li, G. M. Zhu, Z. M. Zhang, J. R. Wang and Q. L. Feng, *Small*, 2023, **19**, 9.
19 W. He, D. Wu, L. L. Kong, P. Yu and G. W. Yang, *Adv. Mater.*, 2024, **36**, 11.
20 U. Celano, D. Schmidt, C. Beitia, G. Orji, A. V. Davydov and Y. Obeng, *Nanoscale Adv.*, 2024, **6**, 2260–2269.
21 K. Kumar, P. Sharma, S. Verma, S. K. Saini, N. K. Tailor, S. Husale, R. K. Singh, S. Satapathi, V. G. Achanta and M. Kumar, *Adv. Funct. Mater.*, 2024, **34**, 16.
22 Y. Wu, Z. Z. Hu, Z. G. Liu, H. L. Zhou, S. Ni, J. Y. Wu, D. Su, Y. J. Song, C. L. Liu, X. Y. Zhang and T. Zhang, *ACS Photonics*, 2024, **11**, 5358–5366.
23 L. H. Zeng, S. H. Lin, Z. J. Li, Z. X. Zhang, T. F. Zhang, C. Xie, C. H. Mak, Y. Chai, S. P. Lau, L. B. Luo and Y. H. Tsang, *Adv. Funct. Mater.*, 2018, **28**, 11.
24 C. Su, M. Y. Li, H. Yan, Y. Zhang, H. Li, W. H. Fan, W. J. Bai, X. J. Liu, Q. G. Wang and S. G. Yin, *ACS Appl. Mater. Interfaces*, 2025, **17**, 5213–5222.
25 C. Guo, C. L. Liu, S. Zhang, C. F. Shi, Z. Q. Z. Chen, X. B. Yu and X. S. Chen, *Opt. Lett.*, 2022, **47**, 4977–4980.
26 L. B. Zhang, Z. Dong, L. Wang, Y. B. Hu, C. Guo, L. Guo, Y. L. Chen, L. Han, K. X. Zhang, S. J. Tian, C. Y. Yao, Z. Q. Z. Chen, M. Cai, M. J. Jiang, H. Z. Xing, X. B. Yu, X. S. Chen, K. Zhang and W. Lu, *Adv. Sci.*, 2021, **8**, 7.
27 L. Wang, J. Wang, C. L. Liu, H. Xu, A. Li, D. C. Wei, Y. Q. Liu, G. Chen, X. S. Chen and W. Lu, *Adv. Funct. Mater.*, 2019, **29**, 10.

28 H. Xu, C. Guo, J. Z. Zhang, W. L. Guo, W. D. Hu, L. Wang, G. Chen, X. S. Chen and W. Lu, *Small*, 2019, **15**, 7.
29 J. Wu, J. Zhang, R. Jiang, H. Wu, S. Chen, X. Zhang, W. Wang, Y. Yu, Q. Fu, R. Lin, Y. Cui, T. Zhou, Z. Hu, D. Wan, X. Chen, W. Hu, H. Liu, J. Lu and Z. Ni, *Nat. Commun.*, 2025, **16**, 564.
30 M. Yu, C. C. Fang, J. F. Han, W. L. Liu, S. M. Gao and K. Huang, *ACS Appl. Mater. Interfaces*, 2022, **14**, 13507–13515.
31 Y. Y. Yu, T. Zhao, M. Peng, T. F. Xu, S. K. Duan, Y. H. She, P. C. Jian, M. H. Chen, Y. Chen, Z. Wang, F. Wu, P. Martyniuk, Y. H. Tsang, B. M. Yao, L. H. Zeng, J. N. Dai, C. Q. Chen and W. D. Hu, *Small*, 2025, **21**, 8.
32 Y. Zhang, K. He, C. Z. Chang, C. L. Song, L. L. Wang, X. Chen, J. F. Jia, Z. Fang, X. Dai, W. Y. Shan, S. Q. Shen, Q. Niu, X. L. Qi, S. C. Zhang, X. C. Ma and Q. K. Xue, *Nat. Phys.*, 2010, **6**, 584–588.
33 M. Q. Che, Y. H. Li, B. Wang, J. Yuan, L. J. Qi, Y. T. Zou, M. X. Liu, X. Y. Zhao, Y. R. Shi, F. Tan, Y. Z. Feng, D. B. Li and S. J. Li, *ACS Photonics*, 2024, **11**, 1693–1702.
34 Y. Lu, Y. Wang, C. Xu, C. Xie, W. Li, J. Ding, W. Zhou, Z. Qin, X. Shen and L.-B. Luo, *Nanoscale*, 2021, **13**, 7606–7612.
35 M. Micica, S. Ayari, M. Hemmat, M. Arfaoui, D. Vala, K. Postava, H. Vergnet, J. Tignon, J. Mangeney, S. S. Guo, X. C. Yu, Q. J. Wang, Z. Liu, S. Jaziri, F. Carosella, R. Ferreira and S. Dhillon, *Adv. Funct. Mater.*, 2025, **35**, 11.
36 S. Y. Zeng, M. M. Zhao, F. Li, Z. H. Yang, H. J. Wu, C. Tan, Q. Sun, L. Yang, L. Lei and Z. G. Wang, *Adv. Funct. Mater.*, 2024, **34**, 10.
37 F. K. Wang, L. G. Li, W. J. Huang, L. Li, B. Jin, H. Q. Li and T. Y. Zhai, *Adv. Funct. Mater.*, 2018, **28**, 10.
38 S. C. Singh, Y. Peng, J. Rudedge and C. L. Guo, *ACS Appl. Electron. Mater.*, 2019, **1**, 1169–1178.
39 Y. X. Zou, Z. K. Zhang, J. W. Yan, L. H. Lin, G. Y. Huang, Y. D. Tan, Z. You and P. Li, *Nat. Commun.*, 2022, **13**, 9.
40 H. B. Zhang, Z. L. Song, D. Li, Y. C. Xu, J. Li, C. J. Bai and B. Y. Man, *Appl. Surf. Sci.*, 2020, **509**, 11.
41 L. H. Zeng, W. Han, S. E. Wu, D. Wu, S. P. Lau and Y. H. Tsang, *IEEE Trans. Electron Devices*, 2022, **69**, 6212–6216.
42 J. D. Yao, J. M. Shao, Y. X. Wang, Z. R. Zhao and G. W. Yang, *Nanoscale*, 2015, **7**, 12535–12541.
43 J. Y. Wu, Y. T. Chun, S. P. Li, T. Zhang, J. Z. Wang, P. K. Shrestha and D. P. Chu, *Adv. Mater.*, 2018, **30**, 7.
44 P. F. Wang, Y. Liu, J. Yin, W. Y. Ma, Z. M. Dong, W. Zhang, J. L. Zhu and J. L. Sun, *J. Mater. Chem. C*, 2019, **7**, 887–896.
45 H. Xu, F. C. Fei, Z. Q. Z. Chen, X. Y. Bo, Z. Sun, X. G. Wan, L. Han, L. Wang, K. X. Zhang, J. Z. Zhang, G. Chen, C. L. Liu, W. L. Guo, L. H. Yang, D. C. Wei, F. Q. Song, X. S. Chen and W. Lu, *ACS Nano*, 2021, **15**, 5138–5146.
46 Z. Dong, W. Z. Yu, L. B. Zhang, H. R. Mu, L. Xie, J. Li, Y. Zhang, L. Y. Huang, X. Y. He, L. Wang, S. H. Lin and K. Zhang, *ACS Nano*, 2021, **15**, 20403–20413.